


Adaptive hierarchical tree algorithm for microlensing wave effect

XIKAI SHAN ^{1,2,3}, GUOLIANG LI^{*},¹ XUECHUN CHEN,^{2,3} AND BIN HU^{2,3}

¹*Purple Mountain Observatory, Chinese Academy of Sciences, Nanjing, Jiangsu, 210023, China*

²*Institute for Frontier in Astronomy and Astrophysics, Beijing Normal University, Beijing, 102206, China*

³*Department of Astronomy, Beijing Normal University, Beijing, 100875, China*

ABSTRACT

The gravitational lensing wave effect generated by the microlensing field embedded in the lens galaxy is an inevitable phenomenon in the realm of strong lensing gravitational waves (SLGW). This effect presents both challenges and opportunities for the detection and application of SLGW. However, investigating this specific wave effect necessitates a complete diffraction integral over each microlens in the field. This operation is very time-consuming because the number of microlenses is very large, ranging from thousands to millions. Therefore, simply adding all of the microlenses is impractical. Additionally, the complexity of the time delay surface makes the lens plane resolution become an important issue that controls the numerical error. In this paper, we propose a trapezoid approximation-based adaptive hierarchical tree algorithm to address the challenges of calculation speed and precision. Our findings demonstrate that this algorithm significantly accelerates the calculation by four orders of magnitude compared to the simple adding method and achieves one order of magnitude acceleration compared to the fixed hierarchical tree algorithm proposed for electromagnetic microlensing. Additionally, our algorithm ensures controllable numerical errors, instilling more confidence in the results. This paper, in conjunction with our previous work (Shan et al. 2023c), comprehensively resolves all numerical issues, including integral convergence, precision, and time consumption. Therefore, this algorithm will greatly facilitate future investigations on the microlensing field wave effect.

Keywords: Gravitational lensing — Diffractional integral — Algorithm — Gravitational wave

1. INTRODUCTION

Strong lensing gravitational waves (SLGW) as a novel probe have demonstrated numerous powerful cosmological applications (Oguri 2019; Bian et al. 2021; Liao et al. 2022), such as precision Hubble constant measurement (Liao et al. 2017), testing modified gravity models (Collett & Bacon 2017; Finke et al. 2021; Narola et al. 2023), and studying the nature of dark matter (Cao et al. 2022; Tambalo et al. 2023a; Seo et al. 2023; Fairbairn et al. 2023). In contrast to the past decade when GW data were too sparse to detect SLGW events, we are now on the verge of its first event detection, especially for binary neutron star lensing events Smith et al. (2023), which will stimulate multi-messenger lensing applications. Therefore, delving deeper into lens modeling

and sub-structure effects is valuable to gain a better understanding of GW lensing and its systematics.

The microlensing field, including stars, remnants, and primordial black holes, constitutes one of the most important components of the lens galaxy. These objects will introduce a unique lensing wave effect on the SLGW generated by stellar mass binary objects (Diego et al. 2019; Meena & Bagla 2020; Mishra et al. 2021), owing to the comparable scale of the lens Schwarzschild radius and the wavelength of the GW (Takahashi & Nakamura 2003). Previous works have demonstrated that the microlensing wave effect is a double-edged sword; from one aspect, it can bias the parameter estimation of SLGW and cause the loss of SLGW identification (Mishra et al. 2023; Shan et al. 2023b), from another side, it can also contribute to the SLGW identification (Shan et al. 2023a). Therefore, conducting more and further studies on the microlensing wave effect will facilitate our understanding of its nature and help find robust methods to convert its disadvantages into advantages. However, the

^{*}Contact e-mail: guoliang@pmo.ac.cn (G. Li);

first important issue that we need to overcome before application is the diffraction integral calculation problem.

In the past thirty years, pioneers have proposed many algorithms to solve this oscillation integral, including contour integration (Ulmer & Goodman 1995), asymptotic expansion methods (Press et al. 1992), Levin’s method (Levin 1982), Filon-type methods (Filon 1930; Xiang 2007; Iserles & Nørsett 2006), and two new hybrid algorithms (Guo & Lu 2020; Tambalo et al. 2023b). However, directly applying these algorithms in the microlensing field scenario is not convenient because there are thousands, even millions, of microlenses in this field, and numerical calculations will encounter convergence, precision, and time-consuming problems inevitably. In our previous work (Shan et al. 2023c), we have solved the convergence problem and advanced the numerical precision using a component decomposition algorithm; however, the resolution of the lens plane and time-consuming problems remain unresolved.

In this paper, we propose an adaptive hierarchical tree algorithm, inspired by the fixed hierarchical tree algorithm designed for the generation of microlensing magnification maps (Wambsganss 1990; Zheng et al. 2022). In Section 2, we will introduce the basic theory of the diffraction integral and our algorithm. In Section 3, we will present the results and compare the acceleration achieved by our algorithm. Finally, in Section 4, we will draw conclusions and discussions.

2. METHOD

2.1. Diffraction integral

In the context of the scalar wave approximation, the gravitational wave (GW) lensing effect can be quantified using the diffraction integral (Schneider et al. 1992; Nakamura & Deguchi 1999; Takahashi & Nakamura 2003) represented by the equation:

$$F(\omega, \mathbf{y}) = \frac{2GM_L(1+z_L)\omega}{\pi c^3 i} \int_{-\infty}^{\infty} d^2x \exp[i\omega t(\mathbf{x}, \mathbf{y})], \quad (1)$$

where $F(\omega, \mathbf{y})$ denotes the amplification factor, and ω and \mathbf{y} represent the GW’s circular frequency and its position (normalized by the Einstein radius) in the source plane, respectively. M_L is the lens mass, z_L is the lens redshift, and \mathbf{x} is the coordinate (normalized by the Einstein radius) in the lens plane. $t(\mathbf{x}, \mathbf{y})$ is the time delay function for the microlensing field embedded in the lens galaxy/galaxy cluster scenario, which is given by (Wambsganss 1990; Schneider et al. 1992; Chen et al.

2021):

$$t(\mathbf{x}, \mathbf{x}^i, \mathbf{y} = 0) = \underbrace{\frac{k}{2} ((1 - \kappa + \gamma)x_1^2 + (1 - \kappa - \gamma)x_2^2)}_{t_{\text{smooth}}(\kappa, \gamma, \mathbf{x})} - \underbrace{\left[\frac{k}{2} \sum_i^{N_*} \ln(\mathbf{x}^i - \mathbf{x})^2 + k\phi_-(\mathbf{x}) \right]}_{t_{\text{micro}}(\mathbf{x}, \mathbf{x}^i)}. \quad (2)$$

Here, $k = 4GM_L(1+z_L)/c^3$, \mathbf{x}^i is the coordinate of the i th microlens, and N_* is the number of microlenses. κ and γ are the macro lensing convergence and shear. $t_{\text{smooth}}(\kappa, \gamma, \mathbf{x})$ and $t_{\text{micro}}(\mathbf{x}, \mathbf{x}^i)$ are the macro lensing and micro lensing time delay, respectively. Here, we set the macro image point as the coordinate origin ($\mathbf{y} = 0$). The contribution from a negative mass sheet, denoted by $\phi_-(\mathbf{x})$, is included to ensure the total convergence κ remains unchanged when adding microlenses (Wambsganss 1990; Chen et al. 2021; Zheng et al. 2022).

However, due to the oscillatory nature of the integrand, conventional Gaussian numerical integration methods are inadequate. To address this limitation, many pioneer works have proposed many algorithms. For example, Levin (1982); Press et al. (1992); Filon (1930); Iserles & Nørsett (2006); Xiang (2007); Guo & Lu (2020); Tambalo et al. (2023b), etc, proposed effective and fast algorithm for isolated microlens, and Ulmer & Goodman (1995) proposed a general algorithm for both isolated and microlensing field. In this paper, we will apply Ulmer & Goodman (1995)’s strategy to solve this oscillation integral. In detail, this algorithm Fourier transforms the amplification factor into the time domain:

$$\tilde{F}(t, \mathbf{y}) \equiv \frac{1}{2\pi} \int_{-\infty}^{\infty} d\omega \exp(-i\omega t) \frac{F(\omega, \mathbf{y})}{C_\omega}, \quad (3)$$

where $\tilde{F}(t, \mathbf{y})$ is the time domain amplification factor and C_ω is the coefficient before the integrand of Eq. (1):

$$C_\omega = \frac{2GM_L(1+z_L)\omega}{\pi c^3 i}. \quad (4)$$

Upon substituting Eq.(1) into Eq.(3), it is evident that the time domain amplification factor is proportional to the time delay probability density function in the lens plane:

$$\tilde{F}(t, \mathbf{y}) = \int_{-\infty}^{\infty} d^2x \delta[t(\mathbf{x}, \mathbf{y}) - t] = \frac{|dS|}{dt}, \quad (5)$$

which can be determined by calculating the surface area dS within the time delay interval dt . The subsequent

step is to inversely Fourier transform $\tilde{F}(t, \mathbf{y})$ to recover $F(\omega, \mathbf{y})$. One can find that this algorithm can efficiently eliminates the oscillation problem.

To calculate the time domain amplification, one direct and straightforward method is to pixelate the lens plane and then accumulate the area of the pixel within the same time delay interval $[t - \Delta t/2, t + \Delta t/2]$ (Diego et al. 2019). This method offers an advantage compared to the contour integration method (Ulmer & Goodman 1995; Mishra et al. 2021). Specifically, this method eliminates the need to identify the image point, where solving a nonlinear lens function is required, which can be time-consuming in the context of the microlensing field scenario. However, this simple adding (refer to as SA in the later of this paper) method needs an extremely high-resolution pixelized lens plane to avoid numerical error induced by the time delay variation in the inner region of the pixel. In other words, if the maximum time delay difference in the pixel is greater than the time delay resolution, rudely arranging the whole pixel area into one time delay interval will introduce numerical error. Therefore, in the case of a highly dense field configuration, the total calculation time,

$$t_{\text{SA}} = N_{\text{pixel}} \cdot N_*, \quad (6)$$

will be very long. Here, N_{pixel} is the total number of pixels in the lens plane and N_* is the number of microlenses.

To reduce the numerical errors induced by the pixels that cross the time delay bins, and meanwhile to speed up the calculation by avoiding an extremely high resolution pixelized lens plane, we propose a trapezoid approximation based adaptive hierarchical tree algorithm. Hereafter, we will refer to this algorithm as TAAH (Trapezoid Approximation based Adaptive Hierarchical) tree algorithm.

2.2. Trapezoid approximation in pixel

The time-domain amplification factor within a pixel can be evaluated through the contour integral:

$$\frac{|dS|}{dt} = \oint_C \frac{ds}{|\nabla_{\mathbf{x}} t(\mathbf{x}, \mathbf{y})|}. \quad (7)$$

Here, ds represents the line element, and C is the length of the iso-time delay curve. The gradient of the time delay can be expressed as:

$$\begin{aligned} \nabla_{\mathbf{x}} t(\mathbf{x}, \mathbf{y}) = & k \begin{pmatrix} 1 - \kappa + \gamma & 0 \\ 0 & 1 - \kappa - \gamma \end{pmatrix} \mathbf{x} \\ & - k \sum_i^{N_*} \frac{\mathbf{x} - \mathbf{x}^{(i)}}{|\mathbf{x} - \mathbf{x}^{(i)}|^2} - k \nabla_{\mathbf{x}} \phi_-(\mathbf{x}), \end{aligned} \quad (8)$$

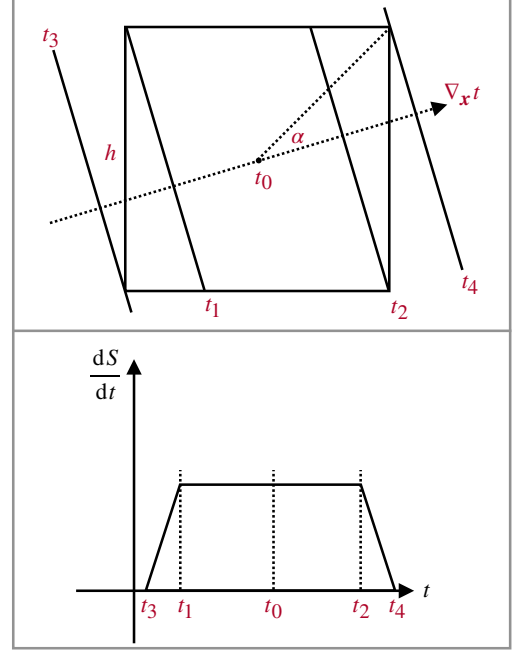


Figure 1. This figure illustrates the time delay gradient (upper panel) and the time domain amplification factor (lower panel) within a sufficiently small pixel that does not include any microlenses. h is the length of the pixel. t_0 represents the time delay at the middle of this pixel, and the straight lines labeled $t_1 \sim t_4$ are the iso-time delay curves. The dashed straight line with an arrow depicts the time delay gradient within this pixel, and α is the angle between the gradient and the diagonal.

and more details can be found in Zheng et al. (2022). It is worth noting that Eq. (8) is differentiable except for the positions of the microlenses. Therefore, the variation of the gradient of the time delay, denoted as $\Delta \nabla_{\mathbf{x}} t(\mathbf{x}, \mathbf{y})$, is finite if the pixel is sufficiently small and does not include any microlenses. Consequently, the gradient of the time delay can be treated as constant in a small enough pixel. Based on this property, we present a sketch that describes the time delay gradient and time domain amplification factor within this type of pixel in Fig. (1).

In the upper panel, we use a black dashed curve with an arrow to represent the gradient of the time delay and use the black solid curves orthogonal to the dashed curve, labeled with different red tags to represent the iso-time delay curves. h is the length of the pixel. t_0 is the time delay in the middle of the square pixel, and α is the angle between the direction of the gradient and the diagonal of the pixel. One can find that the contour length between t_1 and t_2 is constant, and the con-

tour length between t_1 and t_3 and between t_2 and t_4 are monotonically decreasing. Therefore, the time-domain amplification factor within the pixel can be described by:

$$\frac{|ds|}{dt'} = \begin{cases} 0, & t' < t_3 \\ \text{const} \times \frac{t' - t_3}{t_1 - t_3}, & t_3 \leq t' \leq t_1 \\ \text{const}, & t_1 < t' < t_2 \\ \text{const} \times \frac{t - t_2}{t_4 - t_2}, & t_2 \leq t' \leq t_4 \\ 0, & t_4 < t' \end{cases}, \quad (9)$$

where $\text{const} = \frac{h}{\cos(\pi/4 - \alpha) \times |\nabla_{\mathbf{x}} t|}$. The lower panel illustrates this theoretical distribution of the time-domain amplification factor within this pixel.

For pixels that include microlenses, it can be observed that the span of the time delay in such pixels will be infinite. Consequently, the time domain amplification factor within this type of pixel will be zero. Therefore, the trapezoid approximation error in such pixels can be eliminated by reducing the size of the pixel.

After calculating all the time domain amplification factors in all pixels, the final time domain amplification factor at time t in the entire lens plane can be obtained using the formula:

$$\left. \frac{|dS|}{dt} \right|_t = \frac{\sum_{i=0}^{N_{\text{pixel}}} \int_{t-\Delta t/2}^{t+\Delta t/2} \frac{|ds|}{dt'} |_i dt'}{\Delta t}, \quad (10)$$

where i represents the i th pixel, and N_{pixel} is the total number of pixels in the image plane.

2.3. Adaptive hierarchical tree algorithm for diffraction integral

In Section 2.1, we know that the calculation time t_{SA} for the microlensing field diffraction integral is proportional to $N_{\text{pixel}} \times N_*$. This is an unfriendly number especially for the density field. Therefore, it is impossible to rudely sum over all of the microlenses' contribution for each pixel. In this section, we will introduce how our TAAH tree algorithm reduce the time consuming.

The TAAH tree algorithm include two fixed grid levels (Level 1 and Level 2) and an adaptive grid (Level n , $n \geq 2$). The first two fixed grid is based on the algorithm proposed in Zheng et al. (2022), which is focused on the generation of the microlensing magnification map. In detail, the Level 1 grid stores the indices of the microlenses. This grid is used to construction of a lookup table for quickly microlens searching.

Here, we set the resolution of Level 1 as $L_1 = \min\{L_0/10, L_0/\sqrt{N_*}\}$, where L_0 is the length of the total lens plane. $L_0/\sqrt{N_*}$ is the average length that each microlens occupied. This setting ensures that the number of Level 1 pixels is comparable to the number of microlenses when the microlens number is relatively large.

When the number of microlenses is relatively small, we set the length of the Level 1 grid as $L_0/10$. The reason for this choice is that the Level 1 grid is also used to determine whether the microlens is in the far field or near field. This setting ensures the size of the Level 1 grid is not too big to be used as a standard for far/near field microlens decision.

The Level 2 grid stores the deflection angle of the far field microlenses. As outlined in Wambsganss (1990); Chen et al. (2021); Zheng et al. (2022), the evolution of the lens potential induced by far field microlenses within the Level 2 grid is smoothing, and the distance between these microlenses and the center of the Level 2 grid is significantly larger than the resolution of the Level 2 grid. Consequently, the time delay and deflection angle of far field microlenses within the Level 2 grid (in other words, Level n grid in TAAH tree algorithm) can be effectively interpolated using the stored deflection angle (see Wambsganss (1990) for more details). Hence, for a more accurate Level n grid within Level 2, there is no need to recompute the far-field microlenses, and we only need to use the interpolation polynomial to recover its potential. Then, one only needs to sum over the near-field microlenses and add them to the interpolation result to obtain the final result. This leads to a substantial reduction in the total computing time:

$$t_{\text{FH}} \simeq N_{L_2} \cdot N_* + N_{\text{pixel}} \cdot N_{*,\text{near}}, \quad (11)$$

where $N_{L_2} \ll N_{\text{pixel}}$ and $N_{*,\text{near}} \ll N_*$ in a typical microlensing system. Here, we use the same resolution of the Level 2 grid as in Zheng et al. (2022), which is $L_2 = L_1/20$ and far-field microlenses are the lenses outside the nearest eight L_1 grids surrounding the L_1 grid in which the L_2 grid resides (so, the number of near field microlenses $N_{*,\text{near}} \simeq 9$). Eq. (11) is the calculation time for the fixed hierarchical (FH) tree algorithm introduced in Zheng et al. (2022) for the generation of the microlensing magnification map.

The refined grid relative to Level 2 is an adaptive Level n grid, which differs from the Level 3 grid used in Zheng et al. (2022). This choice is inspired by the property of the trapezoid approximation. As established in Section 2.2, the time domain amplification factor within the pixel can be approximated by a trapezoid-shaped distribution. The accuracy of this approximation relies on the relative changing rate of the gradient of the time delay within the pixel. Therefore, if this relative changing rate $|\Delta \nabla_{\mathbf{x}} t|/|\nabla_{\mathbf{x}} t|$ is less than a tiny value ϵ , the approximation is accurate within the tolerance of the error.

Based on this property, we set the length of the level n grid by requiring $|\Delta \nabla_{\mathbf{x}} t|/|\nabla_{\mathbf{x}} t| < \epsilon$. In detail, first,

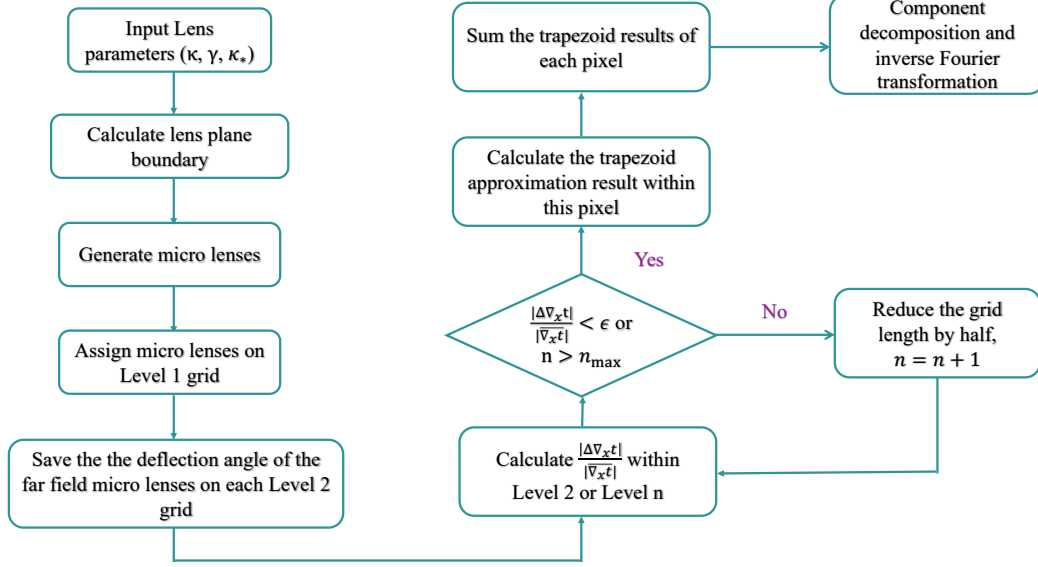


Figure 2. Flow chart of the TAAH tree algorithm.

we calculate $e_2 = |\Delta \nabla_{\mathbf{x}} t| / |\bar{\nabla}_{\mathbf{x}} t|$ in the Level 2 grid. If $e_2 < \epsilon$, the trapezoid approximation in the Level 2 grid is accurate enough, and it does not need further refinement; otherwise, we reduce the grid length by half and calculate $e_n = |\Delta \nabla_{\mathbf{x}} t| / |\bar{\nabla}_{\mathbf{x}} t|$ in each subpixel (where $n \geq 2$ is the resolution level number, and the number of e_n is 4^{n-2}). The refinement stops when all e_n are less than ϵ .

In this process, there are three kinds of special points that will encounter infinite refinement. The first one is our previously mentioned microlens points, the second one is the origin of the lens plane, and the third one is the microlensing image points. In these three kinds of points, the relative difference within the pixel will be ∞ and will not converge by reducing the length of the pixel. To avoid infinite refinement, we set a maximum resolution level n_{\max} to break off the refinement. In the results section, one can find that the numerical error caused by the trapezoid approximation in these three kinds of pixels can be tiny. Up to now, the completed TAAH tree algorithm has been constructed.

In Fig. (2), we present the flow chart of this algorithm, encompassing the following nine main steps:

- Input lens parameters, including macro lensing κ , γ , and micro lensing κ_* .
- Use the method introduced in Shan et al. (2023c) to calculate the microlensing field boundary $L_0/2$.
- Randomly place $N_* = \kappa_* \times L_0^2/\pi$ microlenses within the microlensing field boundary.

- Set Level 1 grid with a length $L_1 = \min\{L_0/10, L_0/\sqrt{N_*}\}$, and assign each microlens to a Level 1 grid.
- Set Level 2 grid with a length $L_2 = L_1/20$, and store the deflection angle contributed by the far field microlenses.
- Calculate $|\Delta \nabla_{\mathbf{x}} t| / |\bar{\nabla}_{\mathbf{x}} t|$ within the Level 2 or Level n grid. If $|\Delta \nabla_{\mathbf{x}} t| / |\bar{\nabla}_{\mathbf{x}} t| < \epsilon$ or $n > n_{\max}$, proceed to the next step; otherwise, reduce the grid length by half and $n = n + 1$.
- Calculate the trapezoid approximation result within the Level n pixel using Eq. (9).
- Sum over the trapezoid approximation results at all Level n grids using Eq. (10).
- Use the Component Decomposition algorithm proposed in Shan et al. (2023c) to recover the frequency domain amplification factor $F(\omega)$.

In the final part of this section, we want to highlight the acceleration of this adaptive algorithm. Compared with the FH tree algorithm (Chen et al. 2021; Zheng et al. 2022) introduced for the generation of the microlensing magnification map, our algorithm does not require a uniformly refined grid over Level 2. Therefore, our algorithm can further accelerate the calculation by reducing the second term of Eq. (11):

$$t_{\text{TAAH}} \simeq N_{L_2} \times N_* + N_{L_n} \times N_{*,\text{near}}, \quad (12)$$

Table 1. This table listed the macro and micro parameters for algorithm precision test. κ and γ are macro lensing convergence and shear, Micro x_1 and Micro x_2 are microlens coordinate. Here, we set the mass of microlens as $100 M_\odot$ for Type I and Type III scenario.

	κ	γ	Micro x_1	Micro x_2
Type I	0.7	0	0.1	0
Type II	0.875	0.325	none	none
Type III	1.3	0	10	0

where N_{L_n} is the total pixel number of the adaptive grid. One can find that if $N_{L_n} \ll N_{\text{pixel}}$, the acceleration will be significant.

$$F(w, \mathbf{x}) = -\frac{1}{\lambda^2 w} 2^{-2-\frac{iw}{2}} |w|^{-1+\frac{iw}{2}} \Gamma\left(1 - \frac{iw}{2}\right) |\lambda|^{-1+\frac{iw}{2}} e^{\frac{iw}{2}(\phi_m + \lambda(x_1^2 + x_2^2))} \left((w + 2i) |\lambda|^3 |w|^3 (x_1^2 + x_2^2) \right. \\ \left. \left(\sinh\left(\frac{\pi w}{4}\right) \text{sgn}(\lambda w) + \cosh\left(\frac{\pi w}{4}\right) \right) {}_2F_3\left(1 - \frac{iw}{4}, \frac{3}{2} - \frac{iw}{4}; 1, \frac{3}{2}, \frac{3}{2}; -\frac{1}{16} \lambda^2 w^2 (x_1^2 + x_2^2)^2\right) \right. \\ \left. - 4\lambda^2 w^2 \left(\cosh\left(\frac{\pi w}{4}\right) \text{sgn}(\lambda w) + \sinh\left(\frac{\pi w}{4}\right) \right) {}_2F_3\left(\frac{1}{2} - \frac{iw}{4}, 1 - \frac{iw}{4}; \frac{1}{2}, \frac{1}{2}, 1; -\frac{1}{16} \lambda^2 w^2 (x_1^2 + x_2^2)^2\right) \right), \quad (13)$$

where $\lambda = 1 - \kappa$, $w = k\omega$ is the dimensionless frequency, Γ and ${}_2F_3$ are gamma function and generalized hypergeometric function.

For Type II macro-lensing images, we exclusively test our algorithm under a pure macro-lensing scenario. This choice is deliberate since logarithmic divergence is Type II's most important characteristic, and there are not analytical solutions when any micro lens is embedded.

Fig. (3) illustrates the resolution level number n (adaptive Level n grid) in the lens plane for three different scenarios, with Type I on the left, Type II in the middle, and Type III on the right. Here, we set $L_2 = 1.024$, $\epsilon = 0.01$, and $n_{\text{max}} = 12$, resulting in a minimum pixel length of $L_{12} = 0.001$. In this figure, the inner region exhibits a higher resolution number, primarily due to macro lensing effects, as $|\Delta \nabla_{\mathbf{x}} t|/|\nabla_{\mathbf{x}} t| \propto 1/|\mathbf{x}|$, where $|\mathbf{x}|$ is the distance from the center. Additionally, the third panel shows that at the micro lens points, the resolution level is very high, as this region is dominated by micro lensing effects and $|\Delta \nabla_{\mathbf{x}} t|/|\nabla_{\mathbf{x}} t| \propto 1/|\mathbf{x} - \mathbf{x}_{\text{micro}}|$, where $\mathbf{x}_{\text{micro}}$ is the coordinate of the micro lenses. This refinement results are aligned with our discussions in Section 2.3.

Fig. (4) illustrates the results of the diffraction integral for the three micro + macro/pure macro lensing configurations. Each column corresponds to a different macro lensing image, with Type I on the left, Type

3. RESULT

3.1. Algorithm precision test

In this section, we evaluate the accuracy of our TAAH tree algorithm by comparing its results with analytical solutions. We consider three distinct macro lensing scenarios, and the corresponding macro and micro lensing parameters are provided in Table 1.

Specifically, for Type I and Type III macro lensing images, we set the shear (γ) value to 0. This choice is made because when a micro lens is embedded in external convergence without external shear, the diffraction has an analytical solution described by:

II in the middle, and Type III on the right. The top (bottom) two rows display the absolute value (phase) of the amplification factor and its relative error between numerical and analytical results. The blue curves represent our TAAH tree algorithm, while the red curves represent the SA algorithm. For the SA algorithm, the resolution at the lens plane was set to 0.001, equivalent to the grid length of the maximum resolution level of the TAAH tree algorithm. It is evident that the precision of our method is comparable to or more accurate than the SA method but requires less time due to the use of fewer pixels at the lens plane. Therefore, the trapezoid approximation can effectively reduce the numerical error arising from the internal time delay variation within the pixel. Here, we do not emphasize the algorithm acceleration, as this is a simple case primarily intended to test our algorithm's accuracy.

3.2. Algorithm acceleration test

In this section, we test the acceleration of the TAAH tree algorithm using realistic microlensing field configurations. Here, we also consider three different macro lensing image types: Type I, Type II, and Type III. The parameters used in the calculations are listed in Table. 2. The lens plane boundary L_0 is determined using the method introduced in Shan et al. (2023c). We choose a precision parameter $\epsilon = 0.1$ and set the max-

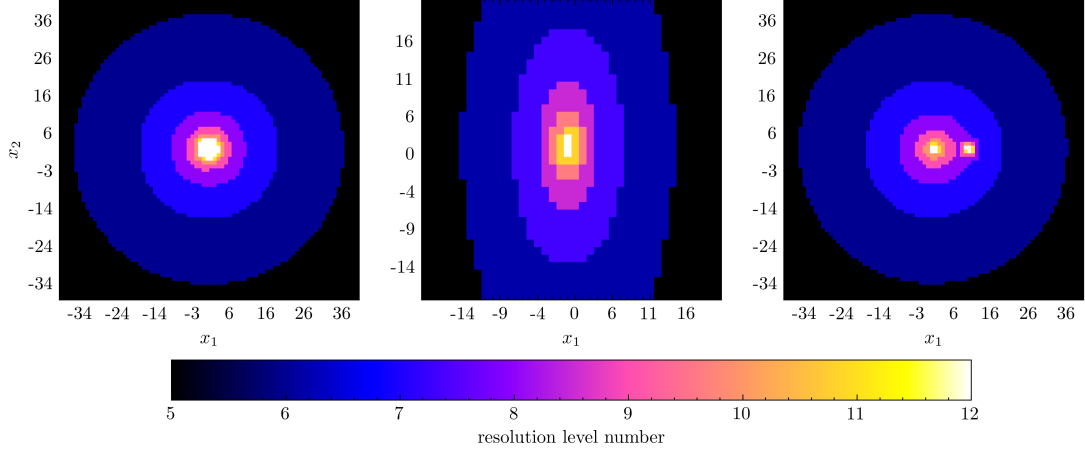


Figure 3. Resolution level number n in the lens plane. Columns from left to right are Type I, Type II and Type III scenarios. The parameters used in these simulations are listed in Table. 1.

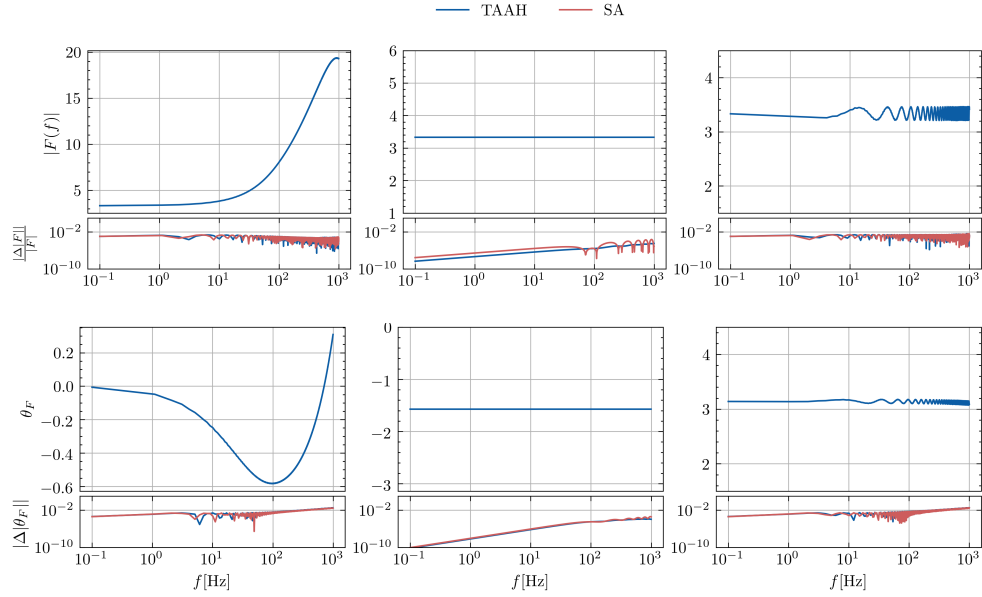


Figure 4. Diffraction integral result for three micro + macro or pure macro lensing scenarios. Each column corresponds to a different macro lensing image, with Type I on the left, Type II in the middle, and Type III on the right. The top (bottom) two rows display the absolute value (phase) of the amplification factor and its relative error between numerical and analytical results. The blue curves represent our TAAH tree algorithm, while the red curves represent the SA algorithm.

imum grid level $n_{\max} = 9$ (resulting in a resolution of $L_9 = L_2/128$).

In Fig. (5), we illustrate the resolution levels for these three macro + micro lensing field configurations. It is evident that the majority of grids are at Level 2 resolution (depicted in black), with only a small portion of the region necessitating higher resolution. As a result, our TAAH tree algorithm can significantly enhance computational efficiency compared to using the FH tree algorithm with a uniformly refined strategy.

In Table. 3, we provide a comparison of calculation times between the SA, FH tree, and TAAH tree algo-

Table 2. This table lists the macro and micro lensing field parameters used in simulations. κ and γ are the macro convergence and shear. κ_* is the microlens convergence. L_0 is the lens plane boundary. ϵ is the precision parameter. Here, we set the mass of the microlens as $1 \text{ M}\odot$.

Parameter	κ	γ	κ_*	L_0	ϵ
Type I	0.7	-0.25	0.06	333.3	0.1
Type II	0.8	0.25	0.06	433	0.1
Type III	1.2	-0.15	0.06	333.3	0.1

rithms. N_{L_2} denotes the pixel number of the Level 2

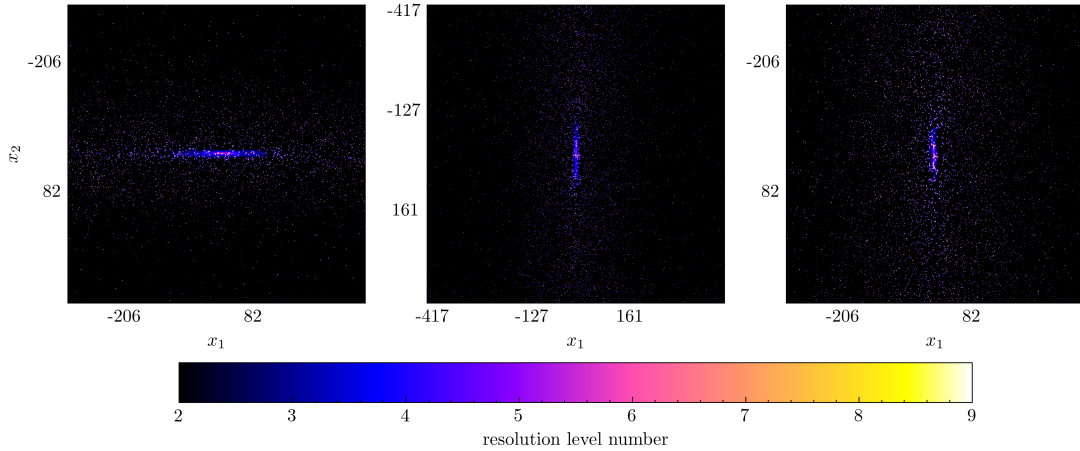


Figure 5. Resolution level numbers for microlensing field scenarios. Columns from left to right represent Type I, Type II, and Type III macro images. The parameters used in these simulations are listed in Table. 2.

grid, N_{L_n} represents the total pixel number ($n > 2$) for the TAAH tree algorithm, and N_{pixel} is the pixel number for the SA and FH tree algorithms, as defined in Eq.(6) and Eq.(11). Here, we set the resolution in the SA and FH tree algorithms equivalent to the minimum resolution in the TAAH tree algorithm, i.e., $L_{\text{pixel}} = L_9$. N_* is the number of microlenses. The sixth column represents the calculation speedup of the TAAH tree algorithm relative to the SA method, and the seventh column represents the calculation speedup of the TAAH tree algorithm relative to the FH tree algorithm.

From this table, it is evident that the TAAH tree algorithm demonstrates a speedup of approximately four orders of magnitude compared to the SA method and approximately one order of magnitude compared to the FH tree algorithm.

In Fig. (6), we compare the diffraction integral results of our TAAH tree algorithm with the FH tree algorithm. Here, we have not presented the results obtained using the SA method due to its excessively long calculation time, making it impractical to complete within a receptive time. In this figure, different columns represent different macro lensing image types, with Type I on the left, Type II in the middle, and Type III on the right. The top (bottom) two rows depict the absolute (phase) value of the amplification factor using TAAH tree algorithm and the differences between TAAH tree algorithm and the FH tree algorithm. One can find that the differences between these two algorithms are less than 1%. Therefore, implementing adaptive refinement over the Level 2 grid based on the trapezoid approximation proves to be highly efficient, achieving both high precision and time savings.

4. CONCLUSION AND DISCUSSION

The gravitational lensing wave effect induced by the microlensing field within the lens galaxy presents both challenges and opportunities for the detection and application of SLGW. Although various algorithms have been proposed by pioneers to address the oscillation diffraction integral (Ulmer & Goodman 1995; Press et al. 1992; Levin 1982; Filon 1930; Xiang 2007; Iserles & Nørsett 2006; Guo & Lu 2020; Tambalo et al. 2023b), applying them directly to the microlensing field scenario remains challenging. This is attributed to the multitude of microlenses in this field, numbering in the thousands, even millions, resulting in numerical calculations inevitably encountering convergence, precision, and time consuming problems.

As a continuation of our prior work (Shan et al. 2023c), where we tackled convergence problems and enhanced numerical precision using a component decomposition algorithm, this paper introduces an adaptive hierarchical tree algorithm based on the trapezoid approximation within the pixel. This algorithm effectively addresses the outstanding challenges related to lens plane resolution and computational time.

In Fig. (4), we compare our TAAH tree algorithm with the theoretical and traditional SA algorithm under a microlens embedded in Type I, Type III, and pure Type II scenarios. Our findings reveal that the TAAH tree algorithm achieves comparable or greater accuracy than the traditional SA algorithm while avoiding the need for high density sampling in the lens plane. More importantly, the TAAH tree algorithm provides a numerical error control method, resulting in more robust result.

Subsequently, we apply our TAAH tree algorithm to the microlensing field scenario. In Fig.(5), we illustrate the resolution levels of the TAAH tree algorithm. We observe that only a small portion of pixels requires refinement relative to the Level 2 grid, leading to accel-

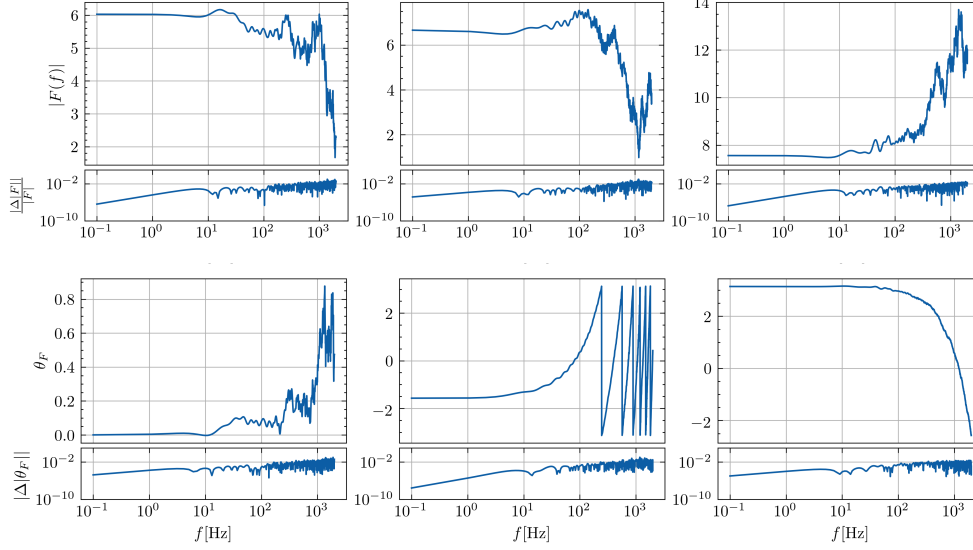


Figure 6. Diffraction integral results for the microlensing field. Columns from left to right represent Type I, Type II, and Type III macro lensing scenarios. The top (bottom) two rows are the absolute (phase) value of the amplification factor using TAAH tree algorithm and the differences between TAAH tree algorithm and the FH tree algorithm. The lens parameters used in these simulations are listed in Table. 2

Table 3. This table lists the grid number and calculation time comparisons between the SA, FH tree, and TAAH tree algorithms. N_{L_2} denotes the pixel number of the Level 2 grid, N_{L_n} represents the total pixel number ($n > 2$) for the TAAH tree algorithm, and N_{pixel} is the pixel number for the SA and FH tree algorithms, as defined in Eq.(6) and Eq.(11). Here, we set the resolution in the SA and FH tree algorithms equivalent to the minimum resolution in the TAAH tree algorithm, i.e., $L_{\text{pixel}} = L_9$. N_* is the number of microlenses. The sixth column represents the calculation speedup of the TAAH tree algorithm relative to the SA method, and the seventh column represents the calculation speedup of the TAAH tree algorithm relative to the FH tree algorithm.

	N_{L_2}	N_{L_n}	N_{pixel}	N_*	$\frac{t_{\text{SA}}}{t_{\text{TAAH}}}$	$\frac{t_{\text{FH}}}{t_{\text{TAAH}}}$
Type I	8.4×10^5	10^8	1.3×10^{10}	8486	1.4×10^4	16
Type II	1.4×10^6	1.6×10^8	2.3×10^{10}	14322	1.5×10^4	10
Type III	8.4×10^5	1.5×10^8	1.3×10^{10}	8486	1.3×10^4	15

erated calculations compared to the FH tree algorithm. As detailed in Table. 3, the TAAH tree algorithm exhibits a four orders of magnitude acceleration compared to the SA algorithm and one order of magnitude acceleration compared to the FH tree algorithm. In Fig. (6), we present the results obtained with the TAAH tree algorithm and the numerical differences between TAAH tree and FH tree algorithms. Our algorithm demonstrates a maximum difference of only 1%.

In summary, we have introduced a novel numerical algorithm for the diffraction integral, specifically tailored for the microlensing field within the lens galaxy. This algorithm effectively resolves numerical resolution challenges and provides control over numerical errors. Furthermore, the incorporation of an adaptive hierarchical

tree algorithm enhances computational efficiency. Consequently, this algorithm holds significant potential for advancing studies on the microlensing wave effect, particularly in the context of density microlensing fields.

- 1 This work is supported by the NSFC (No. U1931210,
- 2 11673065, 11273061). We acknowledge the science re-
- 3 search grants from the China Manned Space Project
- 4 with NO.CMS-CSST-2021-A11, the Sugon Advanced
- 5 Computing service platform for computing support, the
- 6 cosmology simulation database (CSD) in the National
- 7 Basic Science Data Center (NBSDC) and its funds the
- 8 NBSDC-DB-10 (No. 2020000088).

REFERENCES

- Bian, L., et al. 2021, *Sci. China Phys. Mech. Astron.*, 64, 120401, doi: [10.1007/s11433-021-1781-x](https://doi.org/10.1007/s11433-021-1781-x)
- Cao, S., Qi, J., Cao, Z., et al. 2022, *Astron. Astrophys.*, 659, L5, doi: [10.1051/0004-6361/202142694](https://doi.org/10.1051/0004-6361/202142694)
- Chen, X., Shu, Y., Li, G., & Zheng, W. 2021, *The Astrophysical Journal*, 923, 117, doi: [10.3847/1538-4357/ac2c76](https://doi.org/10.3847/1538-4357/ac2c76)
- Collett, T. E., & Bacon, D. 2017, *Phys. Rev. Lett.*, 118, 091101, doi: [10.1103/PhysRevLett.118.091101](https://doi.org/10.1103/PhysRevLett.118.091101)
- Diego, J. M., Hannuksela, O. A., Kelly, P. L., et al. 2019, *Astronomy & Astrophysics*, 627, A130, doi: [10.1051/0004-6361/201935490](https://doi.org/10.1051/0004-6361/201935490)
- Fairbairn, M., Urrutia, J., & Vaskonen, V. 2023, *JCAP*, 07, 007, doi: [10.1088/1475-7516/2023/07/007](https://doi.org/10.1088/1475-7516/2023/07/007)
- Filon, L. N. G. 1930, *Proceedings of the Royal Society of Edinburgh*, 49, 38
- Finke, A., Foffa, S., Iacovelli, F., Maggiore, M., & Mancarella, M. 2021, *Phys. Rev. D*, 104, 084057, doi: [10.1103/PhysRevD.104.084057](https://doi.org/10.1103/PhysRevD.104.084057)
- Guo, X., & Lu, Y. 2020, *Physical Review D*, 102, 124076
- Iserles, A., & Nørsett, S. P. 2006, *BIT Numerical Mathematics*, 46, 549
- Levin, D. 1982, *Mathematics of Computation*, 38, 531
- Liao, K., Biesiada, M., & Zhu, Z.-H. 2022, *Chin. Phys. Lett.*, 39, 119801, doi: [10.1088/0256-307X/39/11/119801](https://doi.org/10.1088/0256-307X/39/11/119801)
- Liao, K., Fan, X.-L., Ding, X., Biesiada, M., & Zhu, Z.-H. 2017, *Nature Communications*, 8, doi: [10.1038/s41467-017-01152-9](https://doi.org/10.1038/s41467-017-01152-9)
- Meena, A. K., & Bagla, J. S. 2020, *Mon. Not. Roy. Astron. Soc.*, 492, 1127, doi: [10.1093/mnras/stz3509](https://doi.org/10.1093/mnras/stz3509)
- Mishra, A., Meena, A. K., More, A., & Bose, S. 2023, <https://arxiv.org/abs/2306.11479>
- Mishra, A., Meena, A. K., More, A., Bose, S., & Bagla, J. S. 2021, *Monthly Notices of the Royal Astronomical Society*, 508, 4869–4886, doi: [10.1093/mnras/stab2875](https://doi.org/10.1093/mnras/stab2875)
- Nakamura, T. T., & Deguchi, S. 1999, *Progress of Theoretical Physics Supplement*, 133, 137, doi: [10.1143/PTPS.133.137](https://doi.org/10.1143/PTPS.133.137)
- Narola, H., Janquart, J., Haegel, L., et al. 2023, <https://arxiv.org/abs/2308.01709>
- Oguri, M. 2019, *Rept. Prog. Phys.*, 82, 126901, doi: [10.1088/1361-6633/ab4fc5](https://doi.org/10.1088/1361-6633/ab4fc5)
- Press, W. H., Vetterling, W. T., Teukolsky, S. A., & Flannery, B. P. 1992, *Numerical Recipes Example Book (FORTRAN)* (Cambridge University Press Cambridge)
- Schneider, P., Ehlers, J., & Falco, E. E. 1992, in *Gravitational Lenses* (Springer), 467–515
- Schneider, P., Ehlers, J., & Falco, E. E. 1992, *Gravitational Lenses*, doi: [10.1007/978-3-662-03758-4](https://doi.org/10.1007/978-3-662-03758-4)
- Seo, E., Li, T. G. F., & Hendry, M. A. 2023, <https://arxiv.org/abs/2311.05543>
- Shan, X., Chen, X., Hu, B., & Cai, R.-G. 2023a, <https://arxiv.org/abs/2301.06117>
- Shan, X., Chen, X., Hu, B., & Li, G. 2023b, <https://arxiv.org/abs/2306.14796>
- Shan, X., Li, G., Chen, X., Zheng, W., & Zhao, W. 2023c, *Sci. China Phys. Mech. Astron.*, 66, 239511, doi: [10.1007/s11433-022-1985-3](https://doi.org/10.1007/s11433-022-1985-3)
- Smith, G. P., Robertson, A., Mahler, G., et al. 2023, *Mon. Not. Roy. Astron. Soc.*, 520, 702, doi: [10.1093/mnras/stad140](https://doi.org/10.1093/mnras/stad140)
- Takahashi, R., & Nakamura, T. 2003, *The Astrophysical Journal*, 595, 1039–1051, doi: [10.1086/377430](https://doi.org/10.1086/377430)
- Tambalo, G., Zumalacárregui, M., Dai, L., & Cheung, M. H.-Y. 2023a, *Phys. Rev. D*, 108, 103529, doi: [10.1103/PhysRevD.108.103529](https://doi.org/10.1103/PhysRevD.108.103529)
- . 2023b, *Phys. Rev. D*, 108, 043527, doi: [10.1103/PhysRevD.108.043527](https://doi.org/10.1103/PhysRevD.108.043527)
- Ulmer, A., & Goodman, J. 1995, *The Astrophysical Journal*, 442, 67, doi: [10.1086/175422](https://doi.org/10.1086/175422)
- Wambsganss, J. 1990, PhD thesis, -
- Xiang, S. 2007, *Numerische Mathematik*, 105, 633
- Zheng, W., Chen, X., Li, G., & Chen, H.-z. 2022, *An Improved GPU-Based Ray-Shooting Code For Gravitational Microlensing*, arXiv, doi: [10.48550/ARXIV.2204.10871](https://doi.org/10.48550/ARXIV.2204.10871)